CABARET solutions on Graphics Processing Units for NASA jets: grid sensitivity and unsteady inflow condition effect

Anton P. Markesteijn and Sergey A. Karabasov
School of Engineering and Material Science, Queen Mary University of London, Mile End Road, London, E1 4NS, UK / GPU-prime Ltd, Cambridge, UK

The GPU CABARET method for solving the Navier-Stokes equations coupled with the Ffowcs Williams –Hawkings scheme for far-field noise predictions is applied for conditions of the NASA SHJAR experiment corresponding to Set Point 3 and 7 in accordance with Tanna's classification. The questions addressed include the sensitivity of the flow and noise spectra solutions to the grid resolution and the inflow condition at the nozzle exit. To study the grid sensitivity, several "hand-made" multi-block curvilinear grids are considered along with a simple hanging-nodes-type grid which was automatically generated with OpenFOAM, which solutions are cross-verified. To study the effect of the inflow jet condition, the flow and noise solutions based on the laminar inflow condition for Set Point 7 case are compared with the same based on modifying the interior nozzle geometry with a turbulence grid to generate the initial unsteadiness inside the nozzle so that both the centerline velocity fluctuations and the jet Mach number at the nozzle exit are preserved in accordance with the experiment. The numerical solutions obtained are compared with the experimental data and reference LES solutions available in the literature.

1. Introduction

Turbulent jet flows and the noise generated by them has been a subject of active research since Lighthill's times, both analytically and experimentally [1-4]. More recently, the same has become a subject of computational modelling using first-principle tools such as Large Eddy Simulations (LES) [5-9] thanks to the rise of computer power and advances in numerical methods for high-speed flow computations. For axisymmetric jet flows, there is an extensive amount of data accumulated in the literature, including the classical experiments described in [2] and [10] and the NASA Small Hot Jet Acoustic Rig (SHJAR) experiments reported in [11]. The latter report comprises an account of a comprehensive experimental campaign over a wide range of jet conditions from subsonic to supersonic speeds and also from unheated to heated jet flows with the Reynolds number based on the jet diameter $O(10^6)$. The main circular nozzle geometry considered in these experiments corresponds to the so-called Small Metal Chevron 000 (SMC000) which is a profiled convergent nozzle of funnel shape.

The NASA experiments include several datasets corresponding to different experimental runs for the same nominal conditions at the nozzle exit, which average was presented as the "consensus" dataset. The flow conditions inside the nozzle were not recorded and the experimental data available include the flow Particle Image Velocimetry (PIV) and the far-field microphone measurement data. Thanks to the availability of both the flow data and the far-field acoustic measurement, the SHJAR database has already attracted attention for validation of LES methods [12-14] as well as hybrid Rynolds Averaged Navier Stokes (RANS)-LES approaches [15-17].

The cold jet flow of the NASA SHJAR database corresponding to Set Point (SP) 7 from the Tanna classification has a very long potential core (~$6.5D_j$, where D_j is the jet diameter) and very thin initial shear layers which are very challenging to accurately capture using LES. This latter could explain

why there are relatively few studies in the LES literature which present a consistent set of results for both the flow solutions and the far-field acoustic predictions for the NASA SP7 case. For example, [15] shows how the lack of grid resolution can lead to 10-20% under-prediction of the potential core length of the jet. [12] revisited this benchmark and undertook a series of LES calculations based on the Roe-type finite-volume LES method equipped with a modern explicit sub-grid-scale model (σ-model) for a range of structured grids from 7 to 84 million cells with including a part of the nozzle geometry. For the two finest grids, 41 and 84 million cells, an excellent (within 5%) agreement with the consensus Particle Image Velocimetry (PIV) data for the meanflow velocity profile and the root-mean-square (r.m.s.) velocity fluctuations was reported. In the same study, far-field acoustic spectra predictions were demonstrated based on the permeable surface formulation of the Ffowcs Williams – Hawkings (FW-H) method [17]. For the 41 and 84 million cell grids, the noise spectra predictions are within 2-3dB from the experiment up to the Strouhal number of St=1-2 for 30^o and 90^o polar angle to the jet flow, where $St=f\ D_j/U_j$, where f is dimensional frequency and U_j is the jet velocity at the nozzle exit. Recently, [16] applied a hybrid RANS/LES method with and without additional synthetic turbulence to enhance the RANS/LES transition on an over-set grid of 106 million cells. This study showed an excellent agreement with the experiment for the meanflow and velocity fluctuations and 2-3dB agreement with the experiment for the noise spectra using a similar FW-H approach.
To summarise, the study [12] proved that very good flow and noise predictions for the NASA SP7 are possible with LES provided that a sufficient grid resolution is reached. The latter implies that the following two problems are solved: the LES grid of a suitable quality is generated and the LES run time required for acoustic integration is affordable.

For the grid generation, many LES simulations based on finite-difference or finite-volume schemes rely on high-quality structured multi-block type meshes since the application of fully unstructured meshes reduces the solution quality. Notable exceptions include [21] and [16] who used low-dissipative finite-difference methods on overset-type grids, which required a modification of the original solvers, and [20] who used body-fitted octree-type grids provided with a special-purpose-built proprietary grid generator. Another limitation of the conventional LES methods which restricts their use for industry-relevant problems is their high computational cost compared to the RANS – based methods. Even for relatively simple nozzle geometries, LES calculations are quite costly. For example, in our calculation [9] of the JEAN nozzle case, which is a single-stream jet at a similar Mach and Re-number conditions to NASA SP7, for a 25 million cell structured grid with the CPU CABARET it takes about 170,000 core hours to run the solution for 400 convective or flow-through Time Units (TUs), where $TU = D_j/U_j$. In [22] the same CPU CABARET was employed for simulations of the Rolls-Royce SILOET jet experiment, which corresponds to a cold static jet case at similar high-speed subsonic flow conditions compared to NASA SP7. For a 21 million cell structured grid, the CABARET SILOET solution takes about 98,000 core hours. These run times can be compared with those for the NASA Set Point 7 case and SMC000 nozzle geometry considered in [15]. In this later case RANS/LES calculations on 6.5 million and 21 million cells required about 94,000 and 280,000 core hours for 500 and 400 TUs, respectively. In the follow-on LES study [12], the same NASA SP7 case was simulated with increasing the grid resolution up to 80 million cells. The run times were not reported but the total solution integration time was decreased which suggests that the computational cost grows fast with the grid size. Given the LES cost increase with the grid size, [12] also argued that a feasible practical strategy for LES-based jet noise predictions could be to merge a coarse-grid LES solution run for a long time and a fine-grid LES solution run for a short time within a certain semi-empirical multiple spectra scheme. Typical run times of advanced hybrid RANS/LES methods on similar high-resolution grids are only marginally shorter compared to LES. For example, the RANS/LES simulation from [16] required 288,000 core hours for the integration time of 205 TUs on a 106 million cell grid for the same SP7 case. Further details of these cases are compared in Table 1 below.

Table 1: Typical computational integration and run times of LES methods

Nozzle	Acoustic Mach number	Grid size, million cells	Integration time, TUs	CPU core x hours
JEAN (Faranosov et al. 2013)	0.75	25	200	512x168
SILOET (Semiletov et al. 2015)	0.875	21	200	2048x48
SMC000 (Xia, 2015)	0.9	6.5	300	72x780
SMC000 (Xia, 2015)	0.9	20.8	200	512x225
SMC000 (Angelino et al. 2016)	0.9	41.1	100	
SMC000 (Angelino et al. 2016)	0.9	84.3	50	
SMC000 (Hussman et al. 2017)	0.9	106	205	906x300

In general, the computational expense of LES calculations is linked to the high degree of concurrency, which is required for the computational method to simulate the wide diversity of temporal scales typical of high-Reynolds number flows. This concurrency requires a high degree of parallelism from an LES code, which becomes challenging to achieve on fully unstructured meshes if the simulation time is a factor. For the conventional MPI CPU implementations of Navier-Stokes solvers, such concurrency can presently only be achieved on large computer clusters.

The expense of conventional Eulerian LES approaches has also become one of the reasons why Lagrangian meshless particle methods such as Lattice Boltzmann have gained popularity in jet aeroacoustics [23]. Thanks to their simplicity, such solvers can also be run in single precision and are highly scalable for parallel computing, hence, they offer an attractive alternative to the conventional Navier-Stokes methods.

In this article, we will use a Eulerian LES method and deal with the problem of unstructured grids and computational concurrency by using the CABARET method combined with hanging node- type meshes and implemented on Graphics Processing Units (GPU). A brief overview of CABARET and its GPU implementation are given below. The original CABARET scheme was introduced as a compact formulation of the second-order Upwind Leapfrog [24,25]. CABARET is an explicit scheme which is second order in space-time. It has superior dispersion and dissipation properties for the schemes of its class. The computational stencil of CABARET takes just one cell in space and time for linear advection which is achieved by using staggered conservation and flux variables that are both defined as "active". Similarly to Lax–Wendroff-type methods, CABARET is fully discrete in space and time. Starting from the original formulation for one dimensional linear advection and scalar conservation laws [26,27] CABARET was extended to aeroacoustics [28], geophysical fluid dynamics [29], and nuclear engineering flows [30]. Details of the CABARET scheme for solving the 3D Navier-Stokes equations in the framework of the MILES approach [31] for high-speed jet modelling as well as the details of its implementation in the curvilinear multi-block meshes with the permeable multiple-closing disk Ffowcs Williams – Hawking (FW-H) method can be found in [9].

To speed up simulations with non-uniform grids that are typically used for viscous flow calculations, CABARET was extended to asynchronous time stepping [32,33]. The idea of asynchronous time stepping compared to the standard global single- or dual-time stepping is to advance the flow solution in each cell in time with its own update rate in accordance with the explicit Courant-Friedrichs-Lewy (CFL) condition without changing the dispersion and dissipation properties of the scheme. Depending on the cell size the grid cells are classed into several "update groups" and the flux conservation is strictly enforced at the synchronisation time step in accordance with the "update group" with the largest time step.

For accuracy, the CABARET stencil needs hexahedral-type meshes where each cell centre corresponds to two grid cell faces opposite each other. In [34,35], CABARET was extended to curvilinear grids with a local refinement, which satisfies the CABARET stencil requirement of having two opposite faces for each cell centre. In the same study, CABARET was implemented to be run on

pure Graphics Processing Units (GPU) by completely re-writing the original algorithms so that all calculations are done on GPUs and only using domain decomposition based on the Message Passing Interface (MPI) protocol in case the amount of memory required exceeds the physical memory of a single GPU card. The local grid refinement was achieved by introducing the nested grids in the azimuthal jet direction (comp. fig1a and fig1b) which, in accordance with [7], plays an important role for the initial shear layer development.

Compared to CPUs, the amount of physical memory available to GPUs typically is biggest problem for GPU computing, as for maximum efficiency all computations need to be performed on the GPU alone. However, thanks to the explicit time-stepping scheme and a very compact computational stencil, the GPU-CABARET solver has been optimised to run LES calculations with a very small memory footprint. Hence, the GPU implementation together with the asynchronous time stepping implementation makes LES studies of jet noise modelling with CABARET possible in a reasonable amount of time using a standard workstation computer. In addition, the CABARET algorithm was further optimized to also work with single precision arithmetic, same as the particle methods, which allows for a further factor of ~2 in memory reduction and a clock speed increase compared to the double precision calculations. The latter development is due to re-arranging the update procedure of the solution variables at the new time level: instead of storing and passing the full flow variables across to the new time step, the new update scheme stores and passes across only the time increments relative to the old time level which are order of the time step of the smallest update group of the asynchronous scheme. Thanks to the latter advances, it is now possible to handle computational grids up to 100 million grid cells on a desktop computer equipped with 4 conventional GPU cards. Further details of the GPU CABARET run times on various grids for the NASA SP7 jet case and SMC000 nozzle geometry will be discussed in Section 2.

In [36,37], the CABARET GPU solver has been extended to include split-hexa meshes of hanging node type. Compared to the nested grids used with CABARET previously, which in case of 2:1 refinement can lead to very skew mesh cells (fig.1b), the hanging node type meshes have a much more Cartesian grid quality (fig.1c).

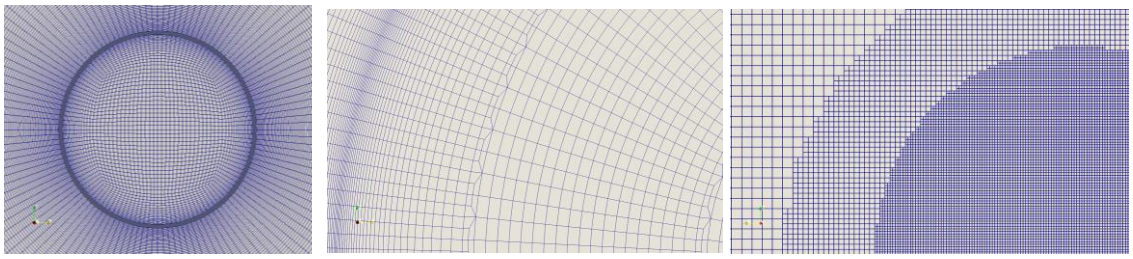

(a) (b) (c)

Figure 1 A typical mesh for the jet cross section: (a) standard multi-block grid, (b) a zoomed-in view of the locally refined grid in the azimuthal direction in the shear layer, (c) an example of how the local refinement can be accomplished with hanging nodes style grid.

The mesh generation is accomplished by using the OpenFOAM utility “snappyHexMesh” (sHM), which is a utility that can generate hexa-dominant meshes automatically from triangulated surface geometries (e.g. CAD geometry). By using sHM and extending CABARET to include hanging nodes, it is possible to generate meshes and solve flow and acoustics for very complicated geometries, while retaining the hexa-dominancy for accuracy. The “snapping” of the mesh to the geometry, can generate a small number of merged non-hexahedral cells such as tetrahedral cells near some elements of the geometry. However, the latter cells are typically less than 1% of the number of boundary cells and for them the CABARET stencil can be replaced by a staggered first-order upwind scheme which option is implemented within the same solver. There is also the option to completely avoid the non-hexahedra cells in the mesh within the same grid generation loop (since OpenFOAM v16.06, June 2016), when the merging of the snapped boundary cells is disabled. Furthermore, there is the possibility to generate refined grid “layers” near the boundaries for (partially) resolving the boundary layer.

The goal of the article is two-fold.

First, we perform a grid sensitivity study between several "hand-made" curvilinear multi-block grids of increasing resolution and a simple hanging-node/ snappy-hex type grid generated automatically with OpenFOAM with sufficiently small cells near the wall, but without fitting of any additional "boundary layers" with the CABARET solver. The question to answer will be: can CABARET on simple non-smooth meshes preserve the low-dissipative and low-dissipative properties for a good accuracy of jet flow and noise solutions? For validation of the numerical solutions, the flow and noise data corresponding to the NASA SHJAR experiment at Set Points 3 and 7 (SP3, SP7) will be used.

Secondly, to explore the flexibility of grid generation offered by the snappy-hex meshes with GPU-CABARET, we will consider a jet nozzle geometry with a realistic turbulence grid inside the nozzle and compare it to the experiment. This will serve to probe the question: how important is the unsteady inflow condition for jet flow development and the subsequent noise generation compared to the laminar inflow condition if the boundary layer inside the nozzle is under-resolved and no wall modelling is attempted?
Note that the second question has already received a substantial attention in the jet noise modelling literature. For example, [8] and [19] showed that the difference between applying the realistic unsteady inflow condition and the simple initial laminar inflow condition could be very large (O(5dB) in terms of the far-field noise spectra) for the jet flows they considered. On the other hand, for other high-speed jet flows such as considered by [7] or in case of [13] and [14], who considered the same SMC000 nozzle geometry as in the current article, there were laminar inflow conditions used which didn't lead to a drastic deterioration of the solution accuracy compared to the experiment either in terms of the far-field noise spectra or noise-sensitive jet flow properties such as the fourth-order velocity correlations.

2. Methods: case parameters and computing details

The SMC000 nozzle used in the NASA SHJAR experiment [11] is a convergent nozzle with a 5 degree conic contraction and a 0.04'' thick lip. The inlet diameter of the nozzle is 6'', and the exit diameter is 2''. It has a lip thickness of 0.05'', an outside face angle of 30^o, and a parallel flow section over the last 0.25'' near the exit.

First, the nozzle is simulated assuming laminar flow conditions inside the nozzle. As discussed in the introduction, the laminar conditions may not be ideal but the boundary layer measurements inside the nozzle were not available from the original experiment [11]. In accordance with a more recent work for the same benchmark [16], an a posteriori estimate of the relevant boundary layer thickness for the SP7 jet case gives $\delta=0.0128\ D_j$, where D_j is the nozzle diameter at the jet exit. In terms of not fully defined jet flow conditions at the nozzle exit, the current situation is similar to the one discussed in [37].

The flow conditions considered corresponding to the Tanna Set Point 3 and 7 [10] are summarised in Table 2. Note that the flow parameters at the jet nozzle exit listed, including the Reynolds number, are the same in the experiment and in the simulation. The potential core is defined by the distance between the nozzle exit and the location in the jet where the jet velocity along the centreline drops to $0.95U_j$.

Table 2: Conditions of NASA jet cases

Set Point	Acoustic Mach number	Jet Mach number	Jet Reynolds number based on D_j, $x10^6$	Approximate length of the jet potential core, D_j	T_j/T_∞	NPR
3	0.5	0.513	0.56	5.5	0.95	1.197
7	0.9	0.985	1	6.5	0.835	1.861

For the initial grid sensitivity study, 4 grids of multi-block type with a gradually increasing resolution in the shear layer location in the azimuthal direction (fig.1c) are considered. The first 3 of them (Grids#1-3) concentrate most of the cells in the shear layer in the jet potential core region to mainly investigate the effect of grid resolution on the jet flow development. For these grids, the total grid cell count increases from 57 to 78 million cells with increase of the azimuthal resolution while keeping the resolution in the stream-wise and the radial direction the same so that the finest grid of this set (Grid#3) corresponds to approximately a uniform Cartesian grid in the initial shear layers. Note that the finest Grid#3 still remains under-resolved with respect to the expected boundary layer thickness for the SP7 jet case (~0.0128 D_j). To limit the total grid count while maintaining a high resolution in the shear layer region, Grid#3 uses a local refinement with 2:1 and even 5:1 cell transition in the azimuthal direction and a coarse grid outside the initial jet region $x/D_j>8$ (comp. with the jet potential core length for SP7 jet conditions x/D_j~6.5). With the lessons learnt from the initial grid sensitivity study, Grid#4 is generated as a trade-off between maintaining a good quality grid in the initial shear layer region (similar to Grid#3) and keeping a moderate grid count (similar to Grid#1) by reducing the axial grid resolution. Compared to the first 3 grids, Grid#4 is also generated with the goal to preserve a suitable resolution outside the initial potential core region for resolving acoustic waves with at least 10 points per wavelengths upto Strouhal, St~1 over the first 20 jet diameters from the nozzle exit for acoustic predictions and upto St ~ 2 over the first 10 jet diameters. Then, a fully unstructured grid based on the snappy-hex mesh grid generation strategy with hanging nodes is applied (Grid#5), which satisfies all 3 conditions: it has a suitable resolution of the jet shear layers and the potential core region, maintains a sufficient grid density in the jet volume for acoustic calculations, and has a moderate total grid count. Compared to the first 4 multi-block type grids, this grid is generated automatically using the OpenFOAM mesh generator. Compared to Grid#4, Grid#5 has a similar resolution in the jet potential core region and then expands by a factor of 2 in cell size increase at x/Dj=10, 15, and 20. The last grid considered in this study is Grid#6 which corresponds to Grid#5 whose upstream nozzle part is replaced by a honeycomb mesh section to simulate the turbulence grid effect. Similar to Grid#5, Grid #6 was generated using the automatic snappy-hex mesh grid generation strategy in OpenFOAM.

The grid details are summarised in Table 3. The same table also shows the corresponding running times of the GPU-CABARET solver for the SP7 jet case (comp. with Table 1). The GPU-CABARET was run on a small cluster of conventional desktop computers. The acceleration provided by 1 GPU compared to 1 CPU core is about 50-80 times depending on the GPU card. The computations were performed on several different architectures of GPUs available at the time. There were three different types of GPU cards used: 2x NVidia Geforce Titan Black Edition (6GB), 1x NVidia Tesla K40 (12GB), and 3x NVidia Geforce GTX1070 (8GB). The first two GPU cards are of an older generation architecture (Kepler) than the GTX1070 (Pascal), and, importantly, have a lower memory clock speed. The single precision CABARET code has a memory footprint of roughly 3 million cells per 1 GB of GPU memory, which number can vary slightly depending on the mesh type. For example, Grid #5, which has 61.2 million cells, needs 20.4 GB of memory, hence can be fitted on 3x GTX1070 cards. However in the case of Grids #2 and #3, the computation was performed on 1xK40 and 2xTitan Black, which in total provides the same 24GB of memory and was completely used up. This also meant that the K40 card had to work harder, as it has more data to handle while its memory clock speed is roughly 1.4 times slower than a Titan Black. This last fact is reflected in the table by the low amount of TUs per day compared to the other cases. The table also shows the additional speed-up gained due to the asynchronous time stepping on each grid compared to the global time stepping. For asynchronous time stepping, the local CFL stability condition is: $|CFL_x|+|CFL_y|+|CFL_y|\sim 0.8$, which is a much more relaxed constraint compared to the same for the global time stepping with CABARET, $Max_{over-all-cells}\left(|CFL_x|+|CFL_y|+|CFL_y|\right)\sim 0.8$, where $CFL_q, q=x,y,z$ is the CFL number based on the cell size and the maximum eigen velocity in the q-coordinate direction. Note that the effective speed-up of the asynchronous time stepping compared to the global time stepping depends on the number of small grid cells relative to the total grid count.

Before starting the integration for statistical post-processing, all simulations were run for 200 TUs to remove the initial solution transients, in accordance with recommendations in the literature [9,15]. For statistical averaging, 200-400 TUs are used in this work, which is also in a broad agreement with the literature (comp. with 200-300 TUs in [15] and 270-1800 TUs in [20]).

Table 3: **Summary of the grid resolutions and run times used for GPU-CABARET simulations**

Grid#	Grid resolution at the lipline at the nozzle exit, ($\Delta x/D_j$, $\Delta r/D_j$, $r\Delta\phi/D_j$)	Grid size, million cells	Number of cells in the lipline region	Integration time	Acceleration due to asynchronous time stepping	Number/type of GPU cards	Run time, TUs/24hrs
1	(0.00591, 0.00591, 0.01227)	57.2	256	200	4	2x Titan Black + K40	80
2	(0.00591, 0.00591, 0.00818)	76.1	384	200	4	2x Titan Black + K40	40
3	(0.00591, 0.00591, 0.00491)	78.1	640	200	4	2x Titan Black + K40	40
4	(0.01772, 0.00591, 0.00491)	58.7	640	200	5	2x Titan Black + K40	80
5	(0.01673, 0.00787, 0.00787)	61.2	~400	400	9.5	3x GTX1070	140
6	(0.01673, 0.00787, 0.00787)	60.7	~400	400	9.5	3x GTX1070	140

3. Results

3.1 Flow solutions

3.1.1. Effect of mesh resolution and jet operating conditions

First, the flow solutions for the SP7 case are considered. As discussed in the introduction, this jet case corresponds to a rather long potential core, which requires a fine grid resolution to capture with LES methods.

Fig. 2 illustrates this point by comparing the GPU-CABARET solutions for the centerline profile of the axial meanflow velocity component as well as the same for the fluctuation of the axial velocity component on Grids #1, #2, and #3. Compared to the experiment (PIV consensus data), Grid #1, which is under-resolved in the azimuthal direction, over predicts the fluctuations at the end of the potential core of the jet. On the other hand, the CABARET solutions on Grid #2 and #3 are in a good agreement with the experiment. This suggests that the CABARET method needs at least 400 cells around the azimuthal jet direction or the cell size of about $0.005\text{-}0.008D_j$ for a sufficient resolution of the initial shear layers in the SP7 jet case. Fig.3 further compares the centerline profiles obtained on Grid #4 and #5, which will be used for acoustic modelling, with the solution obtained on the finest grid (Grid#3) and the experiment. The LES solutions predict the same potential core length as in the experiment within 5%. Note a very good agreement between the three solutions which suggests that their resolution is sufficient to ensure that the main jet dynamics predicted doesn't depend on the grid details. To show how well the consensus PIV data are captured in the present CABARET simulations, the centerline profiles obtained on Grid#5 are compared with the reference LES solutions from [12] in Fig.4. Note a good agreement between the CABARET flow solutions on Grid#5, which roughly contains 61 million cells with the finest reference LES solution obtained on a structured grid of about

84 million cells. A small discrepancy between the CABARET solution and the reference LES solution (as well as with the experiment) is only observed very close to the nozzle exit due to the laminar inflow condition used in the current CABARET simulation.

Grid#4 and Grid#5 are the two meshes for which the CABARET solutions will be analysed further. Along with the jet centerline profiles, which bear an important footprint of the jet dynamics, jet lip-line profiles of the flow solution can provide an important information for acoustics since the shear-layer location is most relevant for noise generation in high-speed jet flows. Hence, Fig.5 compares the lipline profiles of the axial meanflow velocity component and the corresponding velocity fluctuations between the CABARET solutions on Grids 3 and 4 with the consensus PIV data and with the reference 84 million grid LES solution from [12]. Again, the GPU-CABARET solutions are in an excellent agreement with [12] and in a good agreement with the experiment except for a vicinity of the nozzle lip where the PIV data show the drop of turbulent velocity fluctuations below 15% of the value of the jet velocity at the nozzle exit.

To conclude the grid sensitivity section for the SP7 jet case, Fig. 6 shows radial distributions of the axial meanflow velocity component and the corresponding velocity fluctuations on Grid#4 and 5 at several cross-sectional discs at locations x/D_j=4, 8, 12, and 16 compared to the consensus PIV data. Again, the CABARET solutions on both grids agree with each other and with the experiment very well.

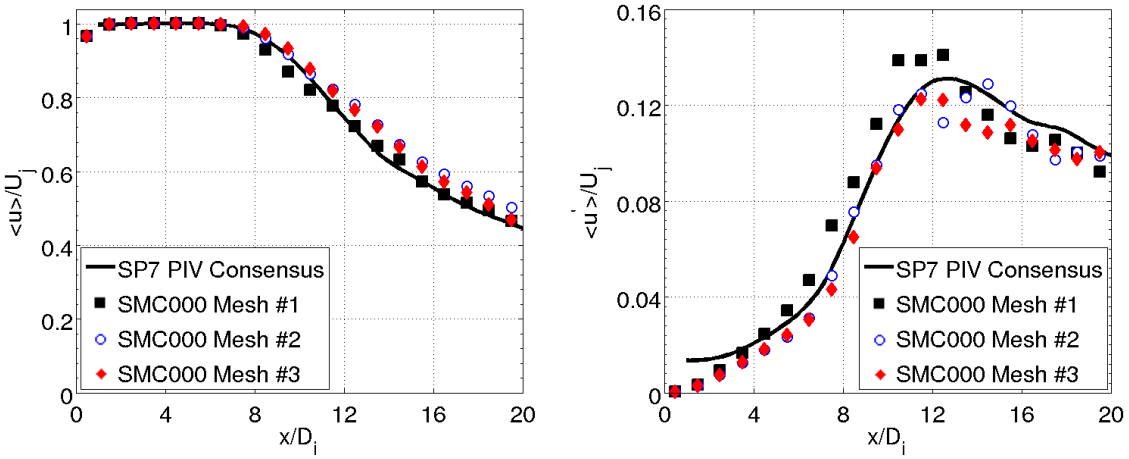

Fig. 2 Jet centreline profiles of mean flow (left) and velocity fluctuations (right) for three different grids with increasing the number of cells in the shear layer and the consensus PIV data for SP7 case from [11].

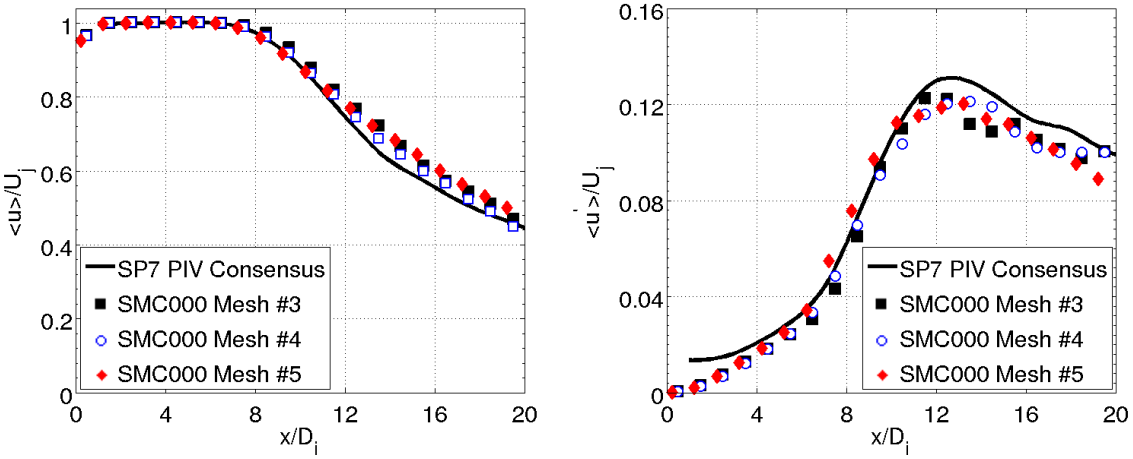

Fig. 3 Jet centreline profiles of mean flow (left) and velocity fluctuations (right) for acoustically optimized meshes #4 and #5, compared to "mean flow-only" mesh mesh #3 and the consensus PIV data for SP7 case from [11].

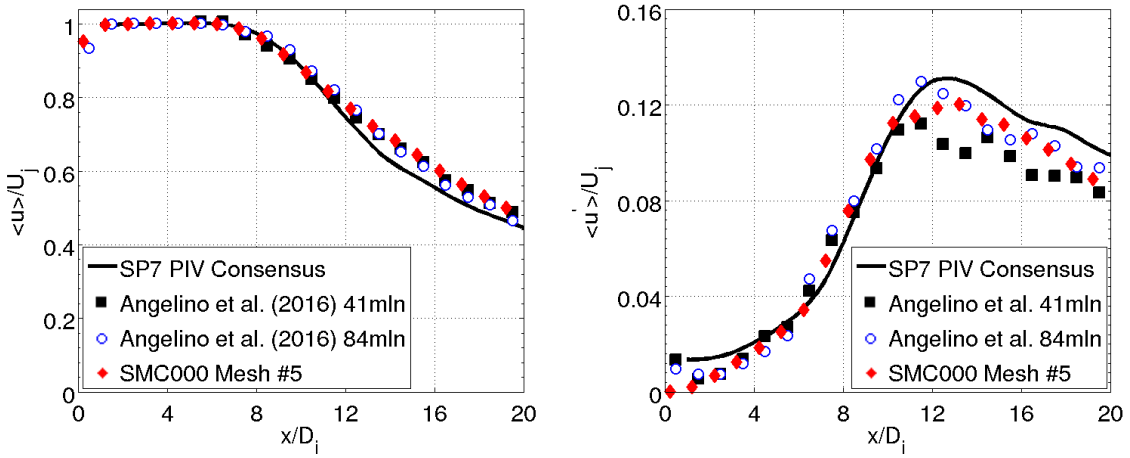

Fig. 4 Jet centreline profiles of the reference LES solutions from [12] for mean flow (left) and velocity fluctuations (right) at the jet-axis (r=0) for the acoustically optimised SMC000 hanging nodes mesh #5, compared to the consensus PIV data for SP7 case from [11].

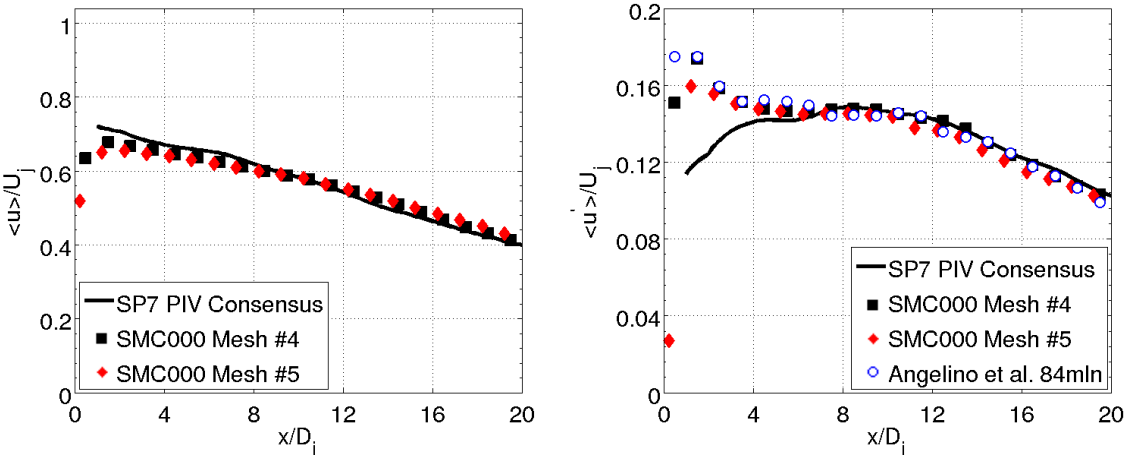

Fig. 5 Jet lip-line profiles for the CABARET solutions on Grid#4 and #5 for mean flow velocity (left) and velocity fluctuations (right) as compared with the reference 84 million cell solution from [12] and the consensus PIV data for SP7 case from [11].

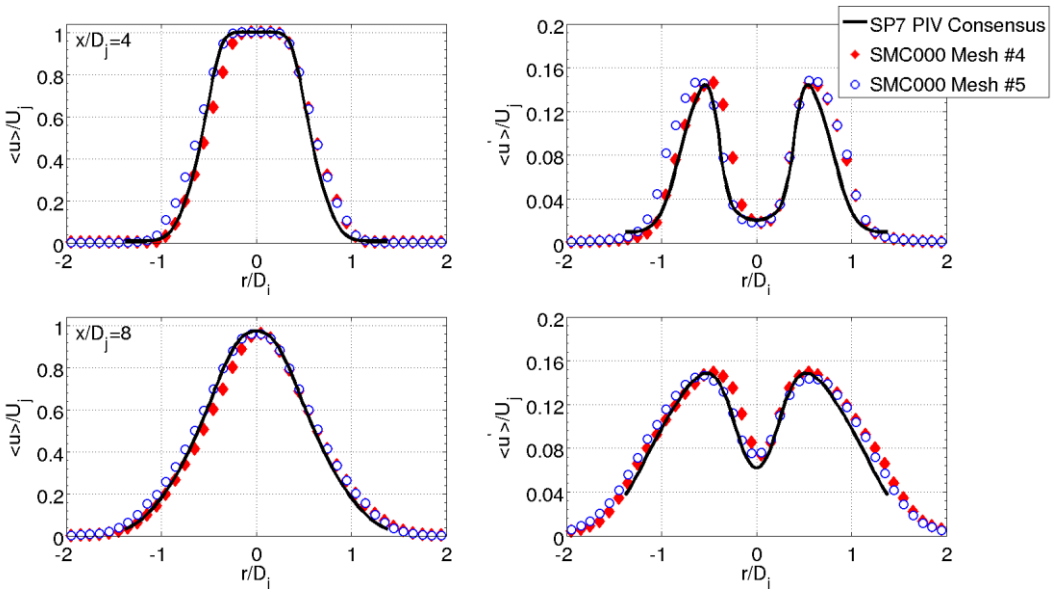

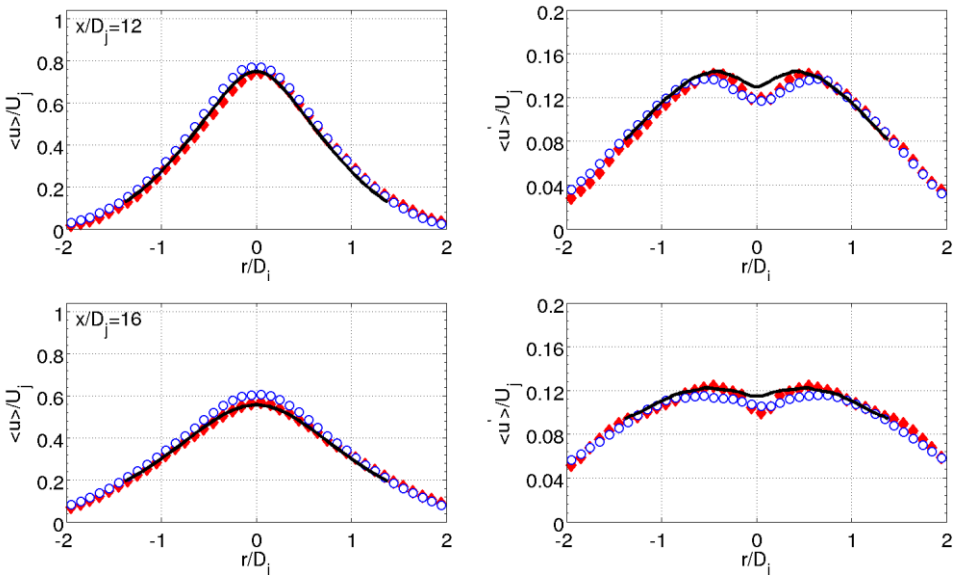

Fig. 6 Radial profiles of mean flow (left) and velocity fluctuations (right) corresponding to the axial velocity component at locations x/Dj=4, 8, 12, and 16 for Grids #4 and #5. The results are compared to consensus PIV data for SP7 case from [11].

To answer the question how sensitive the quality of the CABARET solutions is on Grids #4 and #5 to a change in the jet operating condition without a re-adjustment of the LES grids, the SP3 jet case is considered next. Compared to the SP7 jet, the SP3 jet corresponds to a significantly shorter potential core length (comp. $5.5D_j$ for the SP3 jet with $6.5D_j$ for the SP7 jet), which indicates notable differences in the jet shear later development between the SP3 and the SP7 case considered previously. Again, the LES solutions on both grids predict the same potential core length as in the experiment within 5%. Fig. 7 shows the CABARET solutions for centerline profiles of the axial meanflow velocity component and the corresponding fluctuation on Grid #4 and 5. The LES results are in a good agreement with each other and with the consensus PIV data set for the SP3 jet case. A further comparison with the experiment is shown in Fig. 8 that demonstrates the radial profiles of the axial meanflow velocity and its fluctuations for several cross-sectional discs at x/Dj=4, 8, 12, and 16 shown. Again, same as for the SP7 case, the CABARET solutions on the "automatically generated" Grid#5 are excellent compared to the consensus PIV data for SP3 case. The solutions on Grid#4 for this case show a more variation further downstream from the nozzle exit compared to the experiment. This variation suggests that the "hand-made" Grid#4 whose local refinements were carefully adjusted for the SP7 jet case might not be optimal for the SP3 jet.

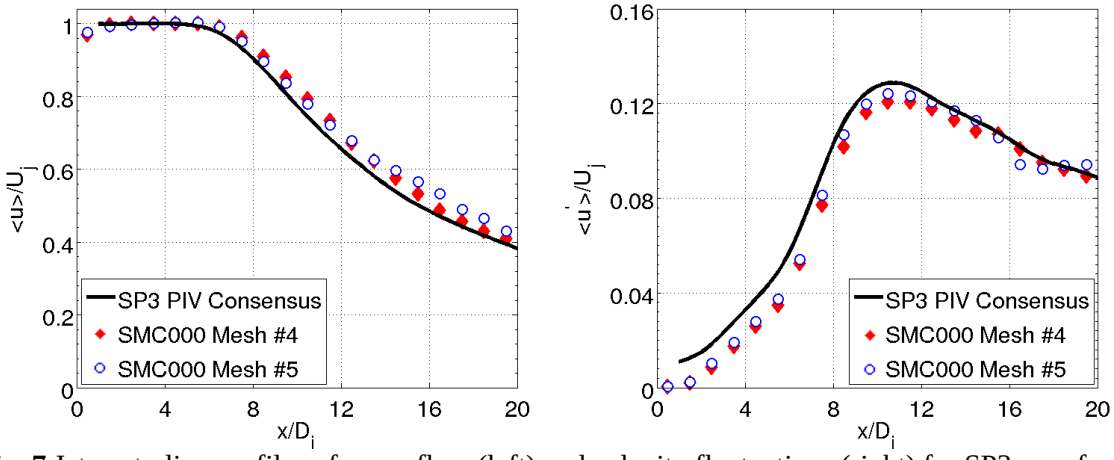

Fig. 7 Jet centreline profiles of mean flow (left) and velocity fluctuations (right) for SP3 case from [11].

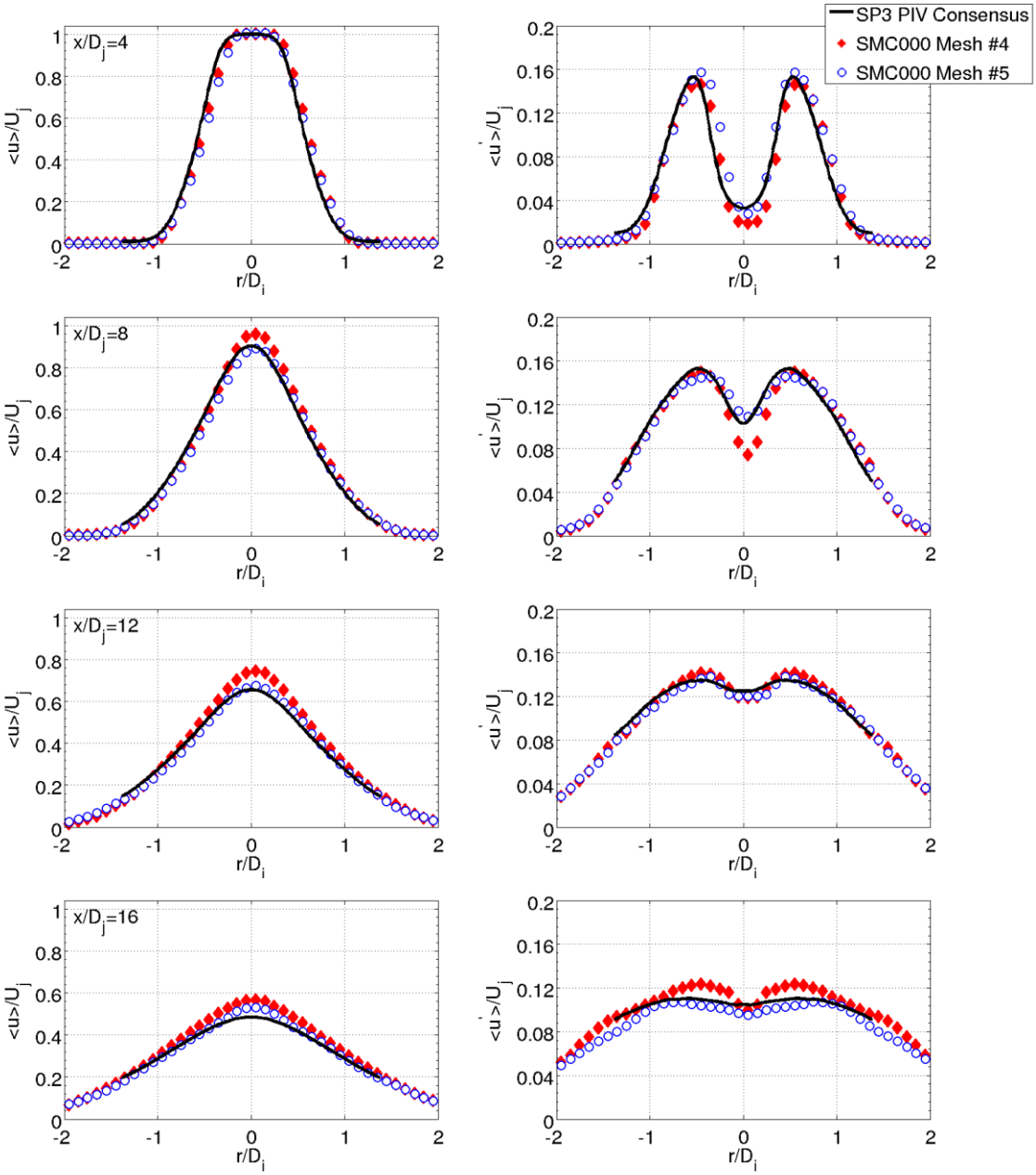

Fig. 8 Radial profiles of mean flow (left) and velocity fluctuations (right) corresponding to the axial velocity component at locations x/Dj=4, 8, 12, and 16 for Grids #4 and #5. The results are compared to consensus PIV data for SP3 case from [11].

3.1.2. Effect of unsteady jet inflow conditions

So far, in all GPU-CABARET simulations a laminar flow inside the nozzle was assumed, that is, no attempt is made to either directly resolve or to model the unsteady flow in the nozzle which results in 1-1.5% turbulent velocity fluctuations at the centre of the nozzle exit in accordance with the consensus PIV data.

To investigate the effect of unsteady flow conditions on the jet development downstream from the nozzle as well as to demonstrate the capability of the current GPU-CABARET solver on snappy-hex meshes, the NASA SP7 jet case is simulated with a generic “honey comb” turbulence grid inserted in the upstream part of the SMC000 nozzle. This modification is implemented in Grid#6 that is completely identical to Grid#5 downstream of the “honey comb” mesh (Fig.9).

This nozzle modification in Grid#6 effectively works like an interior mixer device that generates multiple micro jets which mix out downstream from the turbulence grid in accordance with the governing Navier-Stokes equations. The flow unsteadiness generated leads to a fully 3D flow distribution immediately after the nozzle exit compared to the quasi-2D flow field obtained in the "clean nozzle" case. This difference is demonstrated in Fig.10, which compares the GPU-CABARET solutions on Grids#6 and #5 with and without the turbulence grid inserted, respectively.

The inlet boundary location upstream of the turbulence grid and its location are adjusted so that the resulting acoustic Mach number and the velocity fluctuation at the nozzle exit accurately match the experimental values – 0.9 and 1-1.5%, respectively. The adjustment was done iteratively by performing several runs with the GPU-CABARET solver and analysing the resulting flow solution at the nozzle exit.
Fig. 11 compares the centreline profiles of the axial meanflow velocity component and the corresponding velocity fluctuation for Grid#5 and Grid#6 with the consensus PIV data.
Compared to the "clean nozzle" solution (Grid#5), the inclusion of the turbulence grid in the GPU-CABARET calculation greatly improves the agreement of the turbulent velocity fluctuation profile with the experiment over the first 4 jet diameters from the nozzle exit. The improvement is also notable in comparison with the reference LES solution from [12] who used a different jet inflow condition strategy to match the required level of velocity fluctuations at the nozzle exit (comp. Fig.11 with Fig.5).

However, the difference between the two CABARET solutions with and without including the turbulence grid downstream from the $x/D_j = 4$ location onwards is fairly marginal: both models predict the potential core length of the jet in excess of 6Dj and agree on the peak velocity fluctuation level within 6%. Also, both the LES solutions predict the same potential core length as in the experiment within 5%.

Fig. 12 compares the same profiles of the GPU-CABARET solutions along the lipline, which corresponds to the important location for jet noise. In this case, both the meanflow velocity profiles and the velocity fluctuations corresponding to the turbulence grid and the "clean nozzle" grid are even closer to each other compared to the jet centerline profiles. This suggests that the small flow unsteadiness which was introduced at the nozzle exit in accordance with the NASA experiment for SP7 conditions hasn't resulted in any appreciable change of the jet shear layer development downstream. The question which remains at this point - whether the small changes in the jet development due to the turbulence grid insertion are significant for far-field noise - will be addressed in the next sub-section.

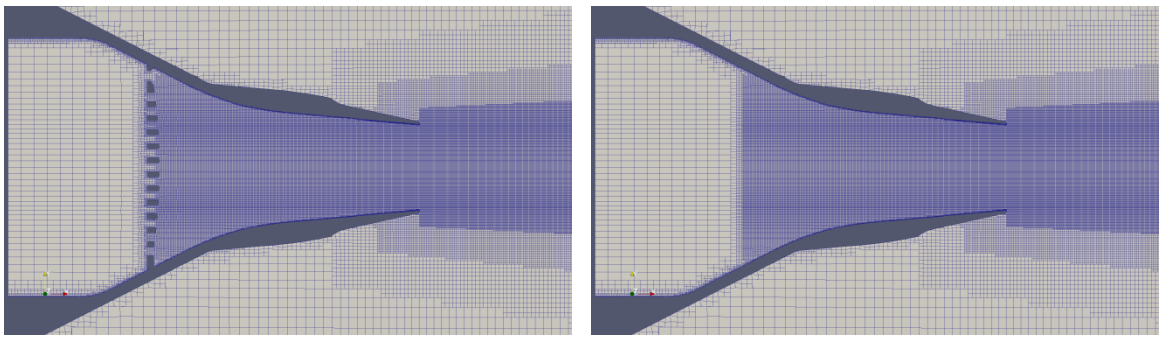

Fig. 9 A rendered view of the SMC000 nozzle with (Grid #6) and without the turbulence grid inside (Grid #5). The mesh was generated using CAD drawings of the SMC000 nozzle and a downloaded STL geometry file of the generic turbulence grid.

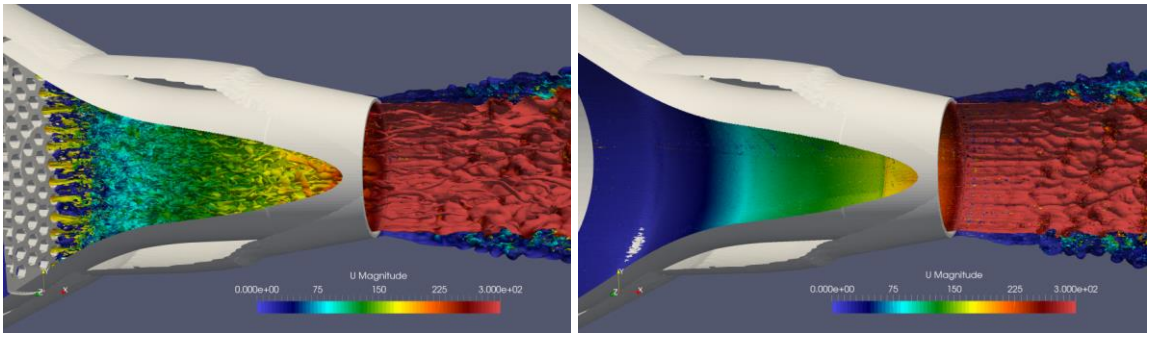

Fig. 10 Instantaneous flow solutions for the SMC000 nozzle simulations with and without the turbulence grid: a 3D iso-surface of vorticity magnitude corresponding to the level |Ω|= 3.2 Uj/Dj and a colour-field of velocity magnitude with 64 linearly distributed levels from 0 to max.

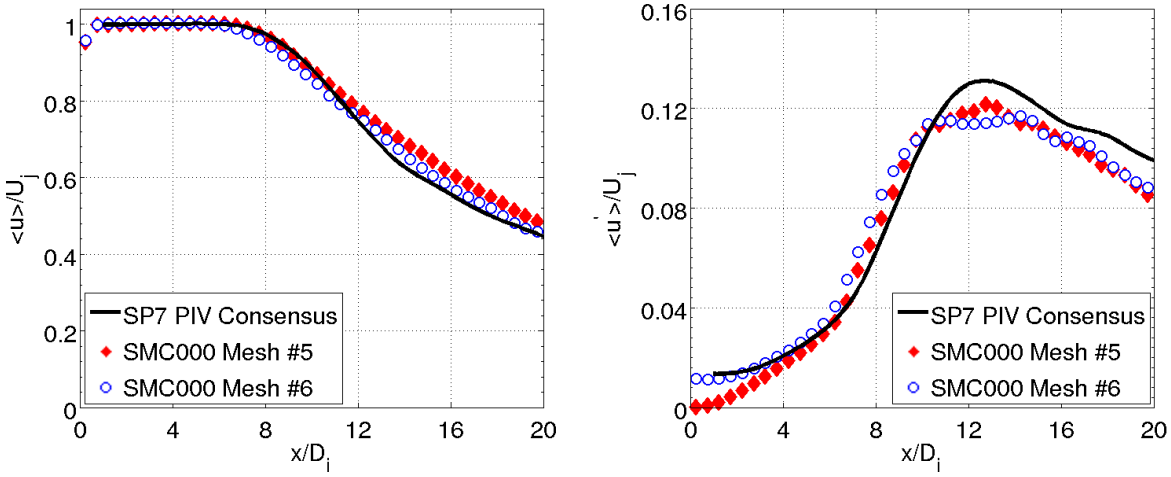

Fig. 11 Jet centreline profiles of mean flow (left) and velocity fluctuations (right) at the centerline of the jet for the SMC000 nozzle with (Grid#6) and without (Grid#5) adding the "honeycomb" turbulence mesh with the consensus PIV data for jet SP7 case from [11].

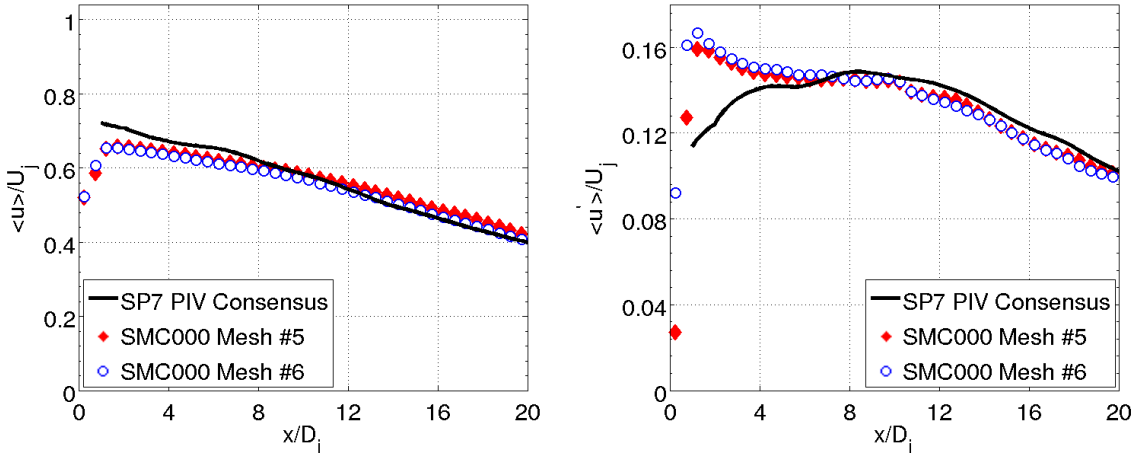

Fig. 12 Jet lipline profiles of mean flow (left) and velocity fluctuations (right) along the lipline of the jet for the SMC000 nozzle with (Grid#6) and without (Grid#5) adding the "honeycomb" turbulence mesh with the consensus PIV data for jet SP7 case from [11].

3.2 Acoustic modelling results
3.2.1 Far-field solution procedure

For far-field sound predictions, the surface integral Ffowcs Williams - Hawkings (FW-H) method [18] based on the penetrable acoustic surface formulation is used. The method is based on computing the acoustic integrands corresponding to the "thickness" and "dipole" terms on a control surface that confines the jet with all important noise sources [39,40] and propagating the solution to the far-field using the analytical free-space Green's function. Under the assumption that all significant noise sources are included inside the control surface, the external quadrupole sources are ignored. Following [5] and [9], several (up to 32 in total) closing discs at about 25 jet diameters downstream from the nozzle exit are used. An average far-field prediction of those obtained with different closing discs was used to filter out the pseudo-sound effect due to vorticity waves crossing the control surface. Upstream of the nozzle exit, the control surface confines the nozzle lip and is left open. Fig.13 shows the location of the control surface with the closing discs (only 4 are shown) and instantaneous jet flow and acoustic solution corresponding to the SP7 jet case on Grid#4. The same acoustic surfaces were used for SP3 case, which corresponds to a shorter potential core of the jet. For the simulations on Grid#5 (and #6) the location of the acoustic surface was slightly altered to adjust to the different grid topology compared to Grid#4, and then the same surface was used for the SP7 and SP3 jet case.

Following [22], for dealing with the finite far-field pressure signal available from the FW-H solution in the time domain, a signal processing technique based on the Welch method [41] is applied. The far-field pressure signal is broken down into several sub-sample intervals with 50%-overlap, each signal sample is Fourier transformed with the Hanning window applied, and the final spectra is obtained by averaging over the intervals available. In the current work 19 and 41 sub-sample intervals are used for the acoustic integration over 200 and 400 TUs.

For noise calculations, the standard sound power spectral density (PSD) and Over All Pressure Level (OASPL) definitions are used that are based on the reference spectra frequency of 1 Hz and reference pressure of 20μPa. The sound propagation angle is calculated with respect to the forward propagation direction in accordance with the convention of the NASA measurements, where the microphone is located on an arch at a distance of 100 D_j from the nozzle exit.

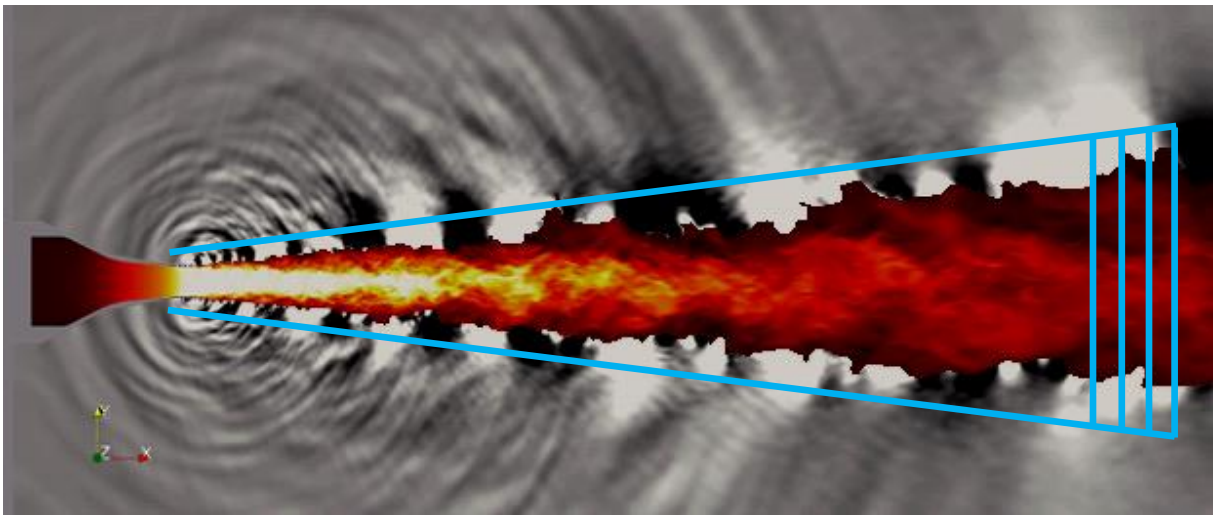

Fig. 13 Location of the acoustic control surfaces relative to the instantaneous absolute velocity and acoustic pressure distributions for the SP7 jet case simulation on Grid #4. The velocity colour scale is linear with 64 levels from 0 to max. The acoustic pressure contours correspond to 64 levels from $0.999p_\infty$ to $1.001p_\infty$.

3.2.2 Acoustic predictions: effect of the grid and the jet operating condition

Fig. 14 compares the far-field spectra predictions obtained on Grid#4 and #5 for the SP7 jet case with the narrowband microphone measurements for a range of microphone angles from 150º to 90º.
The noise predictions on the two grids are in a good agreement with each other and within 2-3dB from the NASA measurements over the frequency range of 0.06<St< 3.

Fig.15 compares the far-field spectra predictions obtained on Grid#4 and #5 for the SP3 jet case with the experiment for the same range of microphone angles. Note that the low frequency predictions at St<0.1 are less good in the SP3 jet case compared to the SP7 jet case. This is likely to be associated with the sensitivity effect of the acoustic integration surface whose location wasn't re-adjusted for the SP3 case. Nevertheless, for frequencies 0.15<St<3, a 2-3dB agreement with the experiment for sound spectra predictions is still obtained.

Fig.16 shows the comparison of acoustics predictions on the same 2 grids for SP7 and SP3 in terms of the OASPL in the frequency band of 0.1<St<3, which demonstrates a 1-2dB agreement with the experiment for the SP7 case and a 0.5-1dB for the SP3 case. The latter accuracy of OASPL predictions is similar to the one reported by [19] who used a wall-modelled LES approach (comp. fig.16 and fig.8 from [19]). The difference in accuracy between the current calculations for SP3 and SP7 is likely to be caused by different numerical grid resolution of the boundary layer which is expected to be thicker for the SP3 case that corresponds to a slower jet compared to SP7.

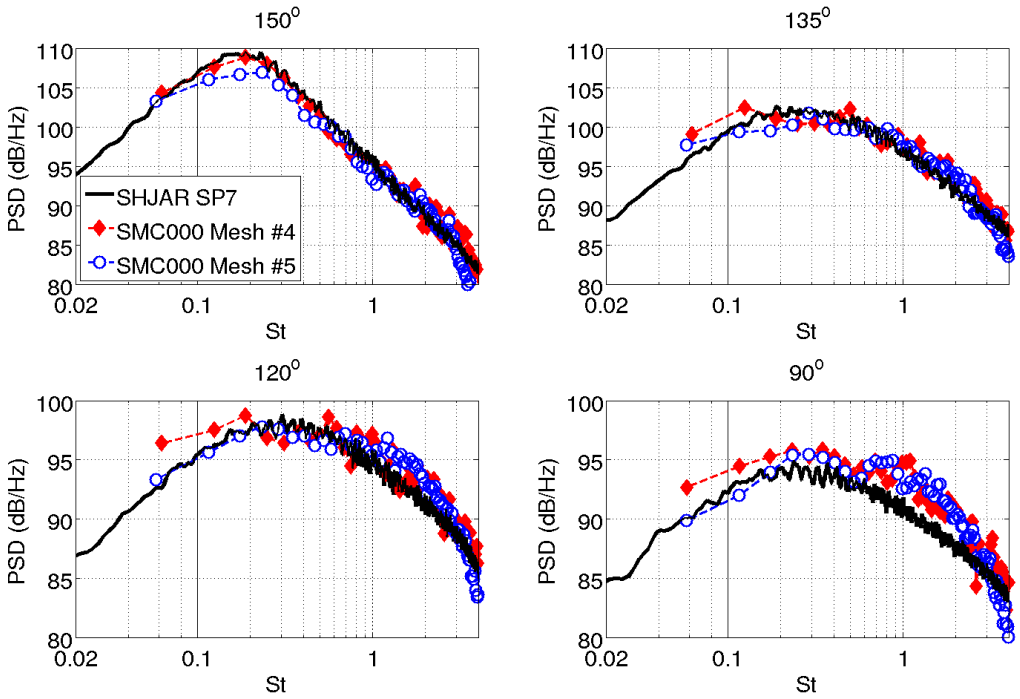

Fig. 14 Far-field sound spectra comparison for Grid #4 and #5 with the experiment for SP7 jet case from [11].

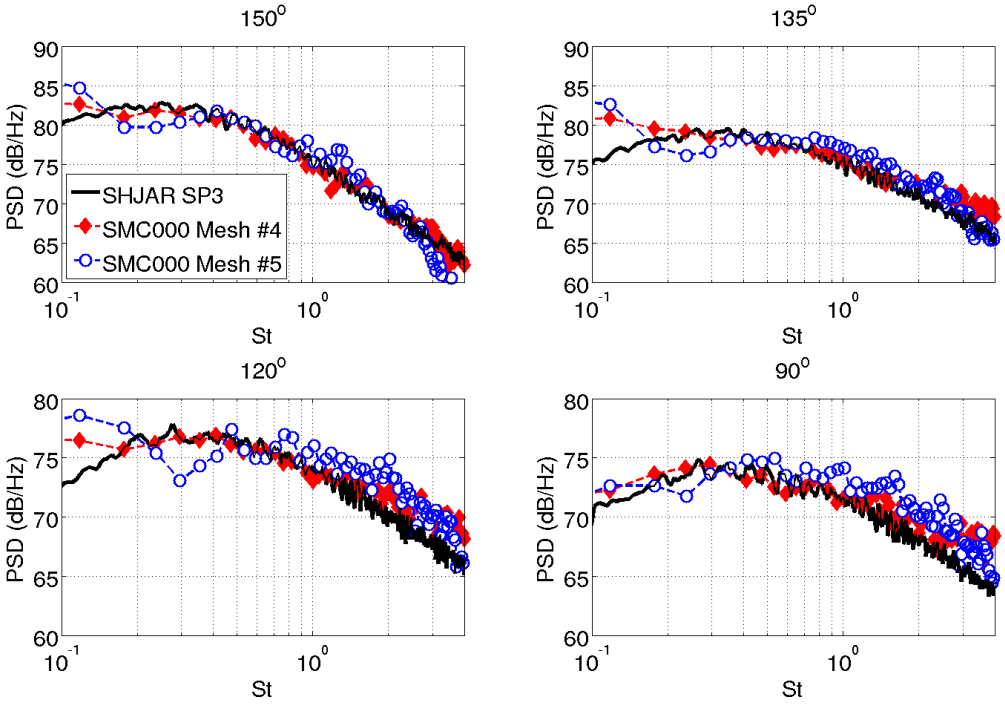

Fig. 15 Far-field sound spectra comparison for Grid #4 and #5 with the experiment for SP3 jet case from [11].

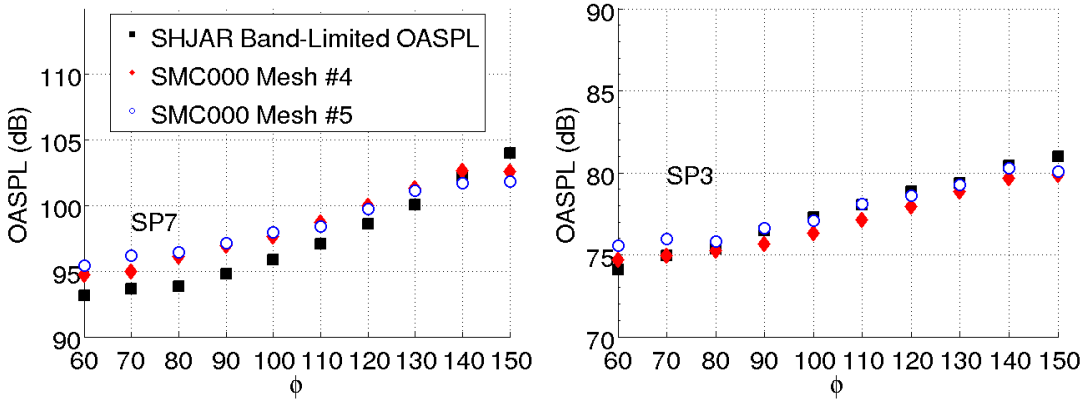

Fig. 16 OASPL comparison for Grid #4 and #5 with the experiment for SP7 (left) and SP3 (right) jet cases from [11].

The overall very good agreement between the acoustic predictions on Grid#4 and #5 with the acoustic measurements is consistent with the results of the grid sensitivity study in section 3.1.1. This also suggests that time window length of 200-400 TUs is sufficient for acoustic integration of the SP7 and SP3 solutions considered.

3.2.3 Effect of the unsteady inflow condition on far-field noise

Finally, the sound prediction for the SP7 jet calculation with the turbulence grid (Grid#6) are considered and compared with the corresponding results for the "clean nozzle" (Grid#5). Fig. 17 shows the corresponding noise spectra comparison with the far-field experiment data. The predictions on the two grids are within 2-3dB one from the other and also the same error bar from the experiment over the frequency range of 0.06<St<3 for all microphone angles from 150º to 90º.

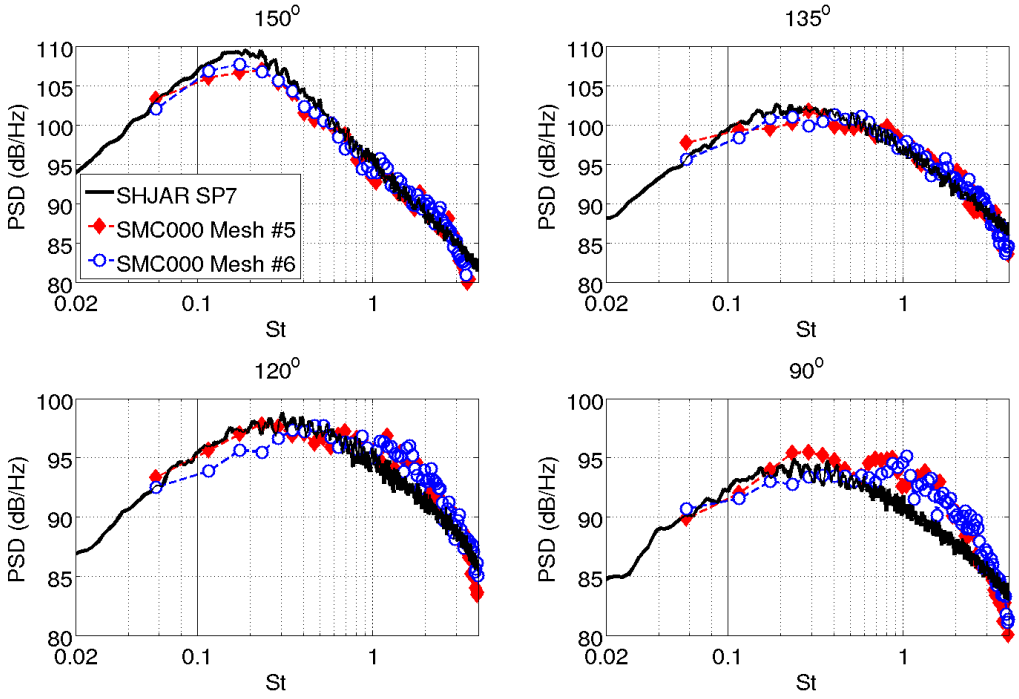

Fig. 17 SPL acoustics results from the SMC000 nozzle SP7 for several observer angles. The results are shown for the nozzle without the "honeycomb" mesh inside the nozzle and when the "honeycomb" is inserted inside the nozzle to trigger the initial flow unsteadiness at the nozzle exit that is observed in the PIV data.

The comparison of the acoustic solutions for OASPL for the frequency band of 0.1<St<3 on the same grids is demonstrated in Fig.18. Here, a 1-2dB agreement between the predictions with and without taking into account the unsteady condition at the nozzle exit with the experiment is observed. Note that the OASPL predictions with and without considering the unsteady condition at the nozzle exit are the same within 0.5dB.

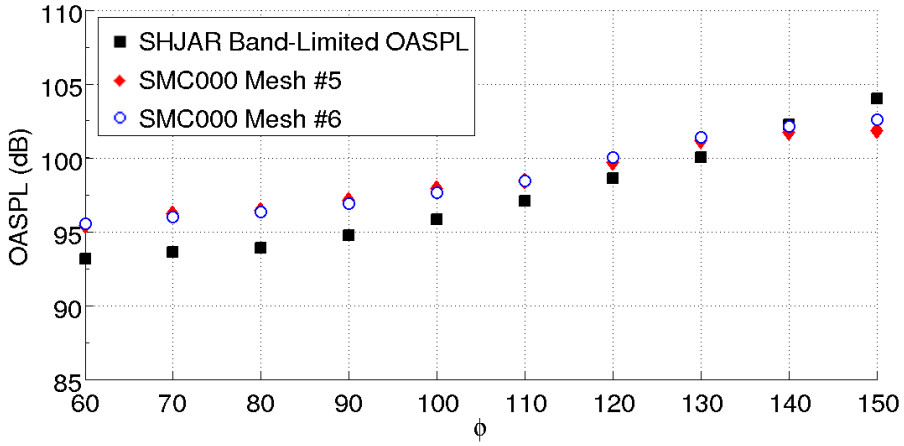

Fig. 18 OASPL comparison for Grid #5 and #6 with the experiment for the SP7 jet case from [11].

The agreement in noise prediction between the simulations produced with the laminar condition at the nozzle exit and the fully unsteady condition that matches the consensus PIV data reinforces the conclusions of section 3.1.2. Indeed, it suggests that the change in the jet inflow condition doesn't result in an appreciable change of the acoustics-sensitive development of the jet in this case.

4. Conclusions

The sensitivity of the new GPU-CABARET solver to the grid resolution and the jet operating conditions has been studied in application to high-speed subsonic jet flow conditions corresponding to Set Point (SP) 7 and 3 of the Tanna classification for the NASA SMC000 nozzle geometry.
It is shown that the CABARET flow solutions on grids circa 60 million cells with a cell size of 0.005-0.008Dj in the initial shear layers are consistently in a very good agreement with the consensus PIV data set from NASA in terms of the meanflow profiles and the velocity fluctuations. All LES solutions predict the same potential core length as in the experiment within 5%. Both the structured multi-block-type and the unstructured grids of hanging-node type generated with OpenFOAM have been tested and produce similar results.
For the most challenging SP7 case, the CABARET solutions on a fully unstructured 60 million cell grid are of a similar quality to those reported in [12] for a 84 million structured grid. Importantly, in addition to the simplicity of mesh generation, the GPU-CABARET solution can be generated at a rate of 140 convective time units per day on a small cluster of desktop computers equipped with only several GPUs.
For far-field acoustic predictions, the GPU-CABARET solver is combined with the Ffowcs Williams – Hawkings (FW-H) method based on a permeable control surface formulation with multiple closing discs. It is shown that the acoustic spectra predictions are within 2-3dB from the experiment for a wide range of microphone angle and frequencies $0.1<St<3$. The OASPL predictions in the frequency band of $0.1<St<3$ agree with the experiment within 1-2dB for the SP7 case and 0.5-1dB for the SP3 case.
To explore the sensitivity of the CABARET predictions to the inflow jet condition, the unstructured grid was modified to insert a realistic turbulence grid upstream of the nozzle exit, which works like an internal mixer device to generate the initial flow unsteadiness. The inlet boundary condition and the location of the turbulence grid were adjusted in order to obtain the same jet Mach number and velocity fluctuations as the reference experiment for the SP7 conditions. This inlet condition modification generated a fully 3D flow at the nozzle exit as visualised from the simulation results and also improved the flow predictions over the first several jet diameters in accordance with the experiment. However, there are no appreciable changes in main jet flow features including the 5% agreement in the length of the potential core with the experiment or far-field noise spectra within 2-3dB error bar or OASPL within 1-2dB error bar compared to the experiment reported due to the modified upstream jet inflow condition. The difference in OASPL predictions between with and without taking the unsteady jet inflow condition into account is 0.5dB. Although these may suggest that, compared to the laminar inflow condition, the introduction of 1-1.5% unsteadiness at the nozzle exit doesn't result in a significant change of the acoustics-sensitive jet shear layer features for the SP7 case, further work will be required to confirm this conclusively based on a more detailed flow analysis and a more resolved flow modelling inside the nozzle. Future work will be devoted to combine the current GPU-LES solver with a wall modelling approach to further refine acoustic predictions for the SP7 case.

Acknowledgments

The authors are grateful to James Bridges for making experimental PIV and acoustic data used for validation in this study readily available. The work of SK has been partly supported by the Engineering and Physical Sciences Research Council (EP/I017747/1) and partly by Aero Acoustic Research Consortium grant with Ohio Aerospace Institute. The authors also gratefully acknowledge the support of NVIDIA Corporation with the donation of the Tesla K40 GPU partly used for this research.

References

1. Lighthill, M. J. On sound generated aerodynamically. I. General theory. Proc. R. Soc. Lond. A, 211(1107):564–587, 1952.
2. Moore, C. J. The role of shear-layer instability waves in jet exhaust noise. J. Fluid Mech., 80:321–367, 1977.

3. Lau, J. C., Morris, P.J. and Fisher, M. Measurements in subsonic and supersonic free jets using a laser velocimeter. J. Fluid Mech., 93:1–27, 1979.
4. Hussein, H.J., Capp, S.P. and George, W.K. Velocity measurements in a high-Reynolds-number, momentum conserving, axisymmetric, turbulent jet. J. Fluid Mech., 258:31–75, 1994.
5. Shur, M. L., Spalart, P. R., Strelets, M. Kh. 2005 Noise Prediction for increasingly complex jets. Part I: Methods and tests. Part II: Applications Int. J. Aeroacoustics, 4(34), 21366.
6. Bodony, D. and Lele, S. K. Current status of jet noise predictions using large-eddy simulation. AIAA J., 46:364–380., 2008.
7. Bogey, C., Mardsen, O., and Bailly, C., "Large-eddy simulation of the flow and acoustic fields of a Reynolds number 105 subsonic jet with tripped exit boundary layers," *Phys. Fluids*, Vol. 23(035104), 2011.
8. Bogey, C., Marsden, O., and Bailly, C. Influence of initial turbulence level on the flow and sound fields of a subsonic jet at a diameter-based Reynolds number of 10^5, J. Fluid Mech. Volume 701, 25 June 2012 , pp. 352-385
9. Faranosov, G. A., Goloviznin, V. M., Karabasov, S. A., Kondakov, V. G., Kopiev, V. F., Zaitsev, M. A. 2013. CABARET method on unstructured hexahedral grids for jet noise computation Computers and Fluids, 88, 165-179.
10. Tanna, H.K. "An experimental study of jet noise: Part I turbulent mixing noise," J. Sound Vib., vol. 50, pp. 405–428, 1977.
11. Bridges, J. and Wernet, M.P., "The NASA Subsonic Jet Particle Image Velocimetry (PIV) Dataset", 2011, NASA/TM-2011-216807
12. Angelino, M., Xia, H., Moratilla-Vega, M. A., and Page, G. J. 2016. Far-feld noise prediction of round and serrated jets with increasingly refined grids. 22nd AIAA/CEAS Aeroacoustics Conference, Lyon, France 30th May- 1st June.
13. Ingraham, D. and Bridges, J. E. "Validating a Monotonically-Integrated Large Eddy Simulation Code for Subsonic Jet Acoustics", 55th AIAA Aerospace Sciences Meeting, AIAA SciTech Forum, (AIAA 2017-0456)
14. Leib, S.J., Ingraham, D., and Bridges, J.E. "Evaluating Source Terms of the Generalized Acoustic Analogy using the Jet Engine Noise REduction (JENRE) Code", 55th AIAA Aerospace Sciences Meeting, AIAA SciTech Forum, (AIAA 2017-0459).
15. Xia, H., 2015. Turbulent jet characteristics for axisymmetric and serrated nozzles. Computers and Fluids, 110, pp. 189-197.
16. Housman, J.A., Stich, G.-D., Kiris, C.C., Bridges, J. Jet Noise Prediction using Hybrid RANS/LES with Structured Overset Grids, 23rd AIAA/CEAS Aeroacoustics Conference 2017, AIAA 2017-3213.
17. Fuchs M., Mockett C., Shur M., Strelets M., Kok J.C. (2018) Single-Stream Round Jet at M = 0.9. In: Mockett C., Haase W., Schwamborn D. (eds) Go4Hybrid: Grey Area Mitigation for Hybrid RANS-LES Methods. Notes on Numerical Fluid Mechanics and Multidisciplinary Design, vol 134. Springer, Cham.
18. Ffowcs Williams, J. E., Hawkings, D. L. 1969 Sound generation by turbulence and surfaces in arbitrary motion Philos. Trans. R. Soc., A264, 32142.
19. Bres, G.A., Jaunet, V., Le Rallic, M., Jordan, P., Colonius, T., and Lele, S.K. "LES for jet noise: the importance of getting the boundary layer right", AIAA Paper 2015-2535.
20. Brès, G., Ham, F.E., Nichols, J.W., Lele, S.K. Unstructured Large-Eddy Simulations of Supersonic Jets, AIAA Journal, Vol. 55, No. 4 (2017), pp. 1164-1184.
21. Marsden, O., Bogey, C., Bailly, C. High-order curvilinear simulations of flows around non-Cartesian bodies, Journal of Computational Acoustics 13 (04), 731-748
22. Semiletov, V., Karabasov, S.A., Chintagunta, A., and Markesteijn, A.P. "Empiricism-free noise calculation from LES solution based on Goldstein generalized acoustic analogy: volume noise sources and meanflow effects", 21st AIAA/CEAS Aeroacoustics Conference, AIAA AVIATION Forum, (AIAA 2015-2536)
23. Casalino, D. and Lele, S. K, Lattice-Boltzmann simulation of coaxial jet noise generation, Center for Turbulence Research, Proceedings of the Summer Program 2014.
24. Iserles, A., Generalized Leapfrog methods. IMA J. Numer. Anal. 1986; 6. 381–392.

25. Roe, P.L., Linear bicharacteristic schemes without dissipation. SIAM J. Sci. Comput. 1998; 19: 1405–1427.
26. Goloviznin, V.M., Samarskii, A.A., Difference approximation of convective transport with spatial splitting of time derivative. Math. Model. 1998; 10:86–100.
27. Karabasov, S.A., and Goloviznin, V. M., Compact accurately boundary-adjusting high-resolution technique for fluid dynamics. J. Comput. Phys. 2009; 228.19: 7426-7451.
28. Karabasov, S.A., and Goloviznin, V.M., New efficient high-resolution method for nonlinear problems in aeroacoustics. AIAA journal 2007; 45.12: 2861-2871.
29. Karabasov, S.A., Berloff, P.S., and Goloviznin, V.M., CABARET in the ocean gyres. Ocean Model. 2009; 30.2: 155-168.
30. Obabko, A.V., Fischer, P.F., Tautges, T.J., Karabasov, S., Goloviznin, V.M., Zaytsev, M.A., Chudanov, V.V., Pervichko, V.A., Aksenova, A.E. CFD validation in OECD/NEA t-junction benchmark. 2011. ANL/NE-11/25.
31. Fureby, C., and Grinstein. F. F., " Large Eddy Simulation of High-Reynolds-Number Free and Wall-Bounded Flows", *Journal of Computational Physics*, 2002, 181, 68-97.
32. Omelechenko, Y.A., Karimabadi, H. A time-accurate explicit multi-scale technique for gas dynamics, Journal of Computational Physics 226, 282-300, 2007
33. Semiletov, V. A., and Karabasov, S. A., "CABARET scheme with conservation-flux asynchronous time-stepping for nonlinear aeroacoustics problems", *Journal of Computational Physics*, 2013, 253(15), 157165.
34. Markesteijn, A.P., Semiletov, V.A., Karabasov, S.A. "CABARET GPU Solver for Fast-Turn-Around Flow and Noise Calculations", 2015, *AIAA-2015-2223*
35. Markesteijn, A.P., Semiletov, V.A., Karabasov, S.A. "GPU CABARET solutions for the SILOET jet noise experiment: Flow and noise modelling", 2016, *AIAA 2016-2967*
36. Markesteijn, A.P. and Karabasov, S.A. "GPU CABARET Solver Extension to Handle Complex Geometries utilizing snappyHexMesh with Asynchronous Time Stepping", 2017, 23rd AIAA/CEAS Aeroacoustics Conference.
37. Markesteijn, A.P. and Karabasov, S.A. "GPU CABARET Solutions for the NASA SHJAR Jet Noise Experiment: Flow and Noise Modeling", 23rd AIAA/CEAS Aeroacoustics Conference, AIAA AVIATION Forum, (AIAA 2017-3852)
38. Bres, G.A., Nichols, J.A., Lele, S.K., Ham, F.E., Schlinker, R.H., Reba, R.A. and Simonich, J.C. Unstructured Large Eddy Simulation of a Hot Supersonic Over-Expanded Jet with Chevrons, 18th AIAA/CEAS Aeroacoustics Conference (33rd AIAA Aeroacoustics Conference) 04 - 06 June 2012, Colorado Springs, CO
39. di Francescantonio, P., "A New Boundary Integral Formulation for the Prediction of Sound Radiation," Journal of Sound and Vibration, Vol. 202, No. 4, 1997, pp. 491–509.
40. Brentner, K. S. and Farassat, F., "Analytical Comparison of the Acoustic Analogy and Kirchhoff Formulation for Moving Surfaces," AIAA Journal, Vol. 36, No. 8, 1998, pp. 1379–1386.
41. Welch, P. D. 1967 The Use of Fast Fourier Transform for the Estimation of Power Spectra: A Method Based on Time Averaging Over Short, Modified Periodograms, IEEE Transactions on Audio Electroacoustics , AU-15, 70-73.